Taylor & Francis
Taylor & Francis Group

Science and Technology of Advanced Materials: Methods

ISSN: (Print) (Online) Journal homepage: www.tandfonline.com/journals/tstm20

NIMS fatigue data sheet on low- and high-cycle fatigue properties of boron steel

Yoshiyuki Furuya, Hideaki Nishikawa & Hisashi Hirukawa

To cite this article: Yoshiyuki Furuya, Hideaki Nishikawa & Hisashi Hirukawa (2024) NIMS fatigue data sheet on low- and high-cycle fatigue properties of boron steel, Science and Technology of Advanced Materials: Methods, 4:1, 2385885, DOI: 10.1080/27660400.2024.2385885

To link to this article: https://doi.org/10.1080/27660400.2024.2385885

Published online: 14 Aug 2024.

SCIENCE AND TECHNOLOGY OF ADVANCED MATERIALS: METHODS
2024, VOL. 4, NO. 1, 2385885
https://doi.org/10.1080/27660400.2024.2385885

Taylor & Francis
Taylor & Francis Group

NIMS fatigue data sheet on low- and high-cycle fatigue properties of boron steel

Yoshiyuki Furuya, Hideaki Nishikawa and Hisashi Hirukawa

Research Center for Structural Materials, National Institute for Materials Science, Ibaraki, Japan

ABSTRACT

The new fatigue data sheet, No. 134, discloses the low- and high-cycle fatigue properties of boron steel. The low-cycle fatigue tests under strain-controlled conditions used incremental step tests to show cyclic stress-strain curves and constant-strain amplitude tests to identify fatigue lives. The incremental step tests reveal that cyclic softening occurs in boron steel; the cyclic yield stress is comparable to that of other steels. The constant-strain amplitude tests revealed three types of fatigue life curves relative to total strain amplitude, plastic strain amplitude and elastic strain amplitude. The crossing points between the plastic strain amplitude curve and the elastic strain amplitude curve were at around 10^3 or 10^4 cycles. The high-cycle fatigue tests comprised uniaxial loading fatigue testing and rotating bending fatigue testing. The high-cycle fatigue strength revealed slight differences between heats that were related to differences in tensile strength. On the other hand, there were only minor differences between the uniaxial loading fatigue test results and the rotating bending fatigue test results. The fatigue strength of the boron steel samples was equivalent to that of low-alloy steel, rather than to that of carbon steel. This resulted from the excellent hardenability of the boron steel samples and indicated high fatigue performance. In the high-cycle fatigue tests, several specimens fractured at over 10^7 cycles without evidence of internal fracturing, so the fatigue limits were not clear. The long-life surface fracturing might be attributable to very mild corrosion effects by air.

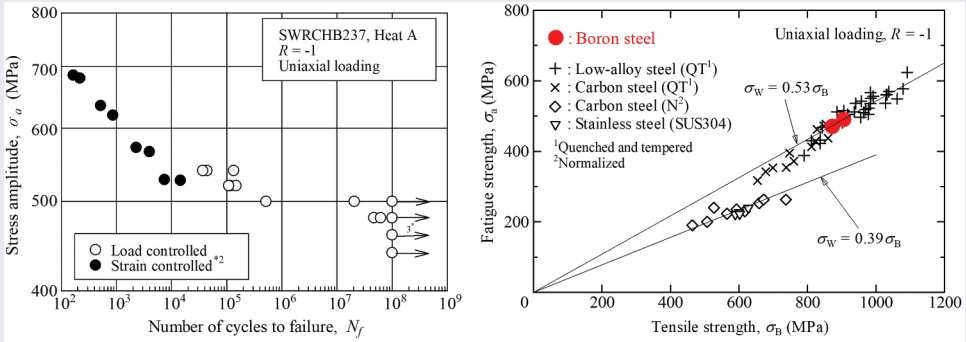

Low- and high-cycle fatigue properties of boron steel

ARTICLE HISTORY
Received 6 May 2024
Revised 27 June 2024
Accepted 24 July 2024

KEYWORDS
Fatigue; structural materials; low- and high-cycle fatigue; boron steel; data sheet

IMPACT STATEMENT

This paper presents a new fatigue data sheet, titled No. 134, on low- and high-cycle fatigue properties of boron steel, followed by the gigacycle and induction-hardened versions.

1. Introduction

NIMS fatigue data sheets comprise a huge database of the fatigue properties of structural materials [1]. The total number of fatigue data sheets is currently 133 (Nos. 0–132). This paper describes a new fatigue data sheet, titled No. 134.

This fatigue data sheet discloses the low- and high-cycle fatigue properties of boron steel. Induction-hardened boron steel is typically used in axles. Our major interest is, therefore, the gigacycle fatigue properties of induction-hardened boron steel. There is, however, as yet no fatigue data sheet on boron steel itself. Its low- and high-cycle fatigue properties therefore need to be clarified. We thus planned two types of fatigue data sheets on boron steel. One is the low- and high-cycle described in this paper. The other is the

CONTACT Yoshiyuki Furuya FURUYA.Yoshiyuki@nims.go.jp Research Center for Structural Materials, National Institute for Materials Science, 1-2-1 Sengen, Ibaraki 305-0047, Japan

gigacycle and induction-hardened version. Gigacycle fatigue tests on induction-hardened boron steel samples are now being conducted using rotating bending fatigue testing.

The low-cycle fatigue tests conducted were of two types. One was a set of incremental step tests [2], which generated cyclic stress-strain curves. The other comprised constant-strain amplitude tests to clarify the fatigue lives. The high-cycle fatigue tests were of the uniaxial loading type and of the rotating bending type at 100 Hz with a cut-off at 10^8 cycles. These fatigue tests were conducted on boron steel samples that had not been induction-hardened. The details of the new fatigue data sheet are as follows.

Table 1. Processing details and related properties of the boron steel samples[1].

Heat	Refining process	Casting process	Product form and size (mm)
A	Al-Si deoxidized	Continuous Casting	Bar φ30
B	Al-Si deoxidized	Continuous Casting	Bar φ20

[1]Sampled in 2021.

Table 2. Chemical composition of the boron steel samples.

	Heat		Elements (mass %) C	Si	Mn	P	S	B
Product analysis	A		0.39	0.19	0.82	0.01	0.014	0.0021
	B		0.39	0.24	0.83	0.013	0.012	0.0019
	Requirement[1]	max	0.40	0.35	0.90	0.030	0.030	
		min	0.34	0.10	0.60			0.0008

[1]JIS G 3508–1 (2010), 'Boron steel for cold heating-Part 1: wire rods'.

Table 3. Heat treatment conditions of the boron steel samples.

Normalizing	Quenching	Tempering
855°C, 0.5 h, air cooled	855°C, 0.5 h, oil quenched	550°C, 1 h, water cooled

Table 4. Mechanical properties of the boron steel samples.

	Tensile properties[1]						
Heat	0.2% proof stress (MPa)	Tensile strength (MPa)	True fracture stress[2] (MPa)	Elongation (%)	Reduction of area (%)	Charpy Impact value[3] (J/cm^2)	Vickers hardness (HV196N)
A	760	873	1640	20	65	204	286
B	832	906	1681	21	66	176	286

[1]JIS Z 2241 (2011), No.14A type specimen with 6 mm diameter and 30 mm gauge length.
The (nominal) strain rate of the specimen was controlled to 0.0008 s^{-1}.
[2]True fracture stress = Fracture load/Minimum cross-sectional area at fracture.
[3]JIS Z 2242 (2018), No. 3 type specimen with 2 mm U-notch, tested at 23 ± 5°C.

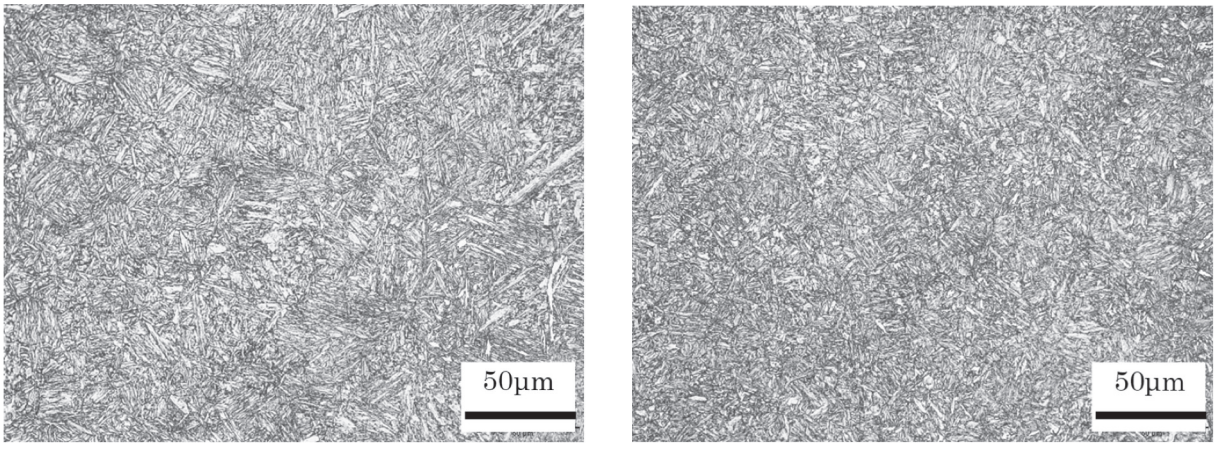

Figure 1. Microstructures of boron steel samples etched in a solution comprising 100 ml ethanol and 3 ml nitric acid.

2. Experimental method

2.1. Materials

Tables 1 and 2 show the processing details and chemical compositions of the tested steel. The tested steel consisted of hot-rolled round bars that had been sampled in 2021. Tables 3 and 4 show the heat treatment conditions and their mechanical properties. The steel was oil-quenched and tempered, resulting in a tensile strength of around 900 MPa. Figures 1 and 2 show the microstructures, which consisted of tempered martensite with prior austenite grain sizes of around 20 μm. There are many etch pits (black circular-shape objects) in Figure 2a, since this sample needed heavy etching to visualize the prior austenite grain boundaries.

2.2. Fatigue testing

Table 5 shows the low-cycle fatigue test conditions. The tests were conducted using servo-hydraulic fatigue testing machines under strain-controlled

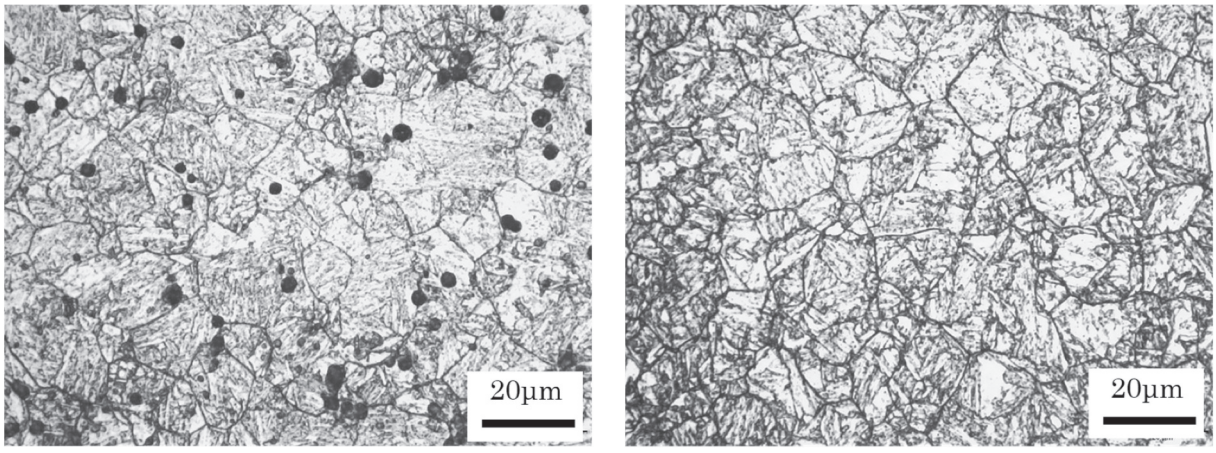

Figure 2. Prior austenite grains of boron steel samples etched in a solution consisting of 500 ml saturated picric acid, 5 ml oxalic acid, 4 ml hydrochloric acid, and 20 g sodium dodecylbenzene sulfonate.

Table 5. Low-cycle fatigue test conditions.

Type of test	Uniaxial
Type and capacity of testing machine	Servo hydraulic type 75 kN
Loading condition	Strain control under zero mean strain
Waveform	Incremental step test[1] 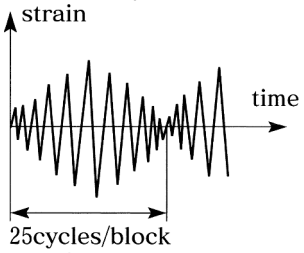 Constant amplitude test 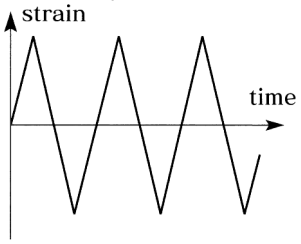
Strain rate	Triangular 5×10^{-3} s^{-1}
Environment	RT (21～25 °C), laboratory air
Specimen[a] (dimensions in mm)	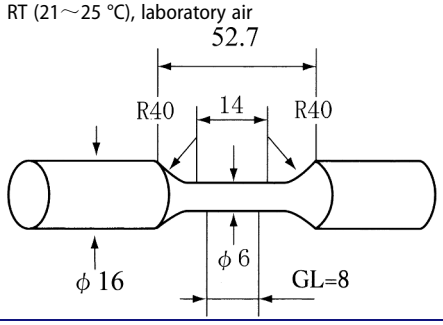

[1]Landgraf, R. W., Morrow, J. and Endo, T.; J. Materials, 4 (1969), 176–188.
[a]The surface was polished longitudinally with 1200 grade silicon carbide paper.

Table 6. High-cycle fatigue test conditions.

Type of test Type and capacity of testing machine	Uniaxial load Electromagnetic resonance 100 kN	Rotating bending 4-point loading type 100 N·m
Loading condition Waveform	Constant amplitude test under zero mean stress 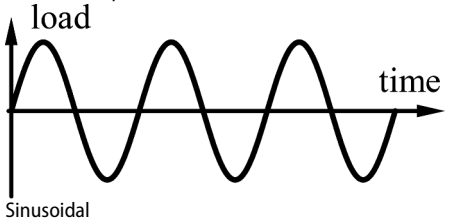 Sinusoidal	
Frequency	100 Hz	
Environment	RT (21 - 25 °C), ambient air	
Specimen[1] (dimensions in mm)	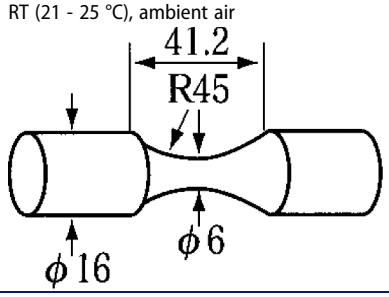	90% risk volume = 227 mm^3 (uniaxail load) = 34 mm^3 (rotating bending)

[1]The surface was polished longitudinally with 1200-grade silicon carbide paper.

conditions. The strain-controlled tests used triangular waveforms with a strain rate of 5×10^{-3} s^{-1}. Both incremental-step and constant-strain amplitude tests were carried out. The incremental step tests employed waveforms in which the strain amplitude was gradually changed, in repeating 25-cycle blocks.

Table 6 shows the high-cycle fatigue test conditions. The uniaxially loaded high-cycle fatigue tests were conducted using an electromagnetic resonance fatigue testing machine under load-controlled conditions. The stress ratio was $R = -1$. The rotating bending fatigue tests were the 4-point bending type. The uniaxial loading and rotating bending fatigue tests used the same configuration of specimens. The high-cycle fatigue tests were conducted up to 10^8 cycles at 100 Hz.

The fatigue tests were conducted in air at room temperature. The specimens were round bar types with minimum diameters of 6 mm. Their surfaces were finished off by longitudinal polishing using 1200-grade silicon carbide papers.

3. Experimental results

3.1. Low-cycle fatigue test results

Figure 3 shows the cyclic stress-strain curves obtained in the incremental step tests. The stress amplitudes

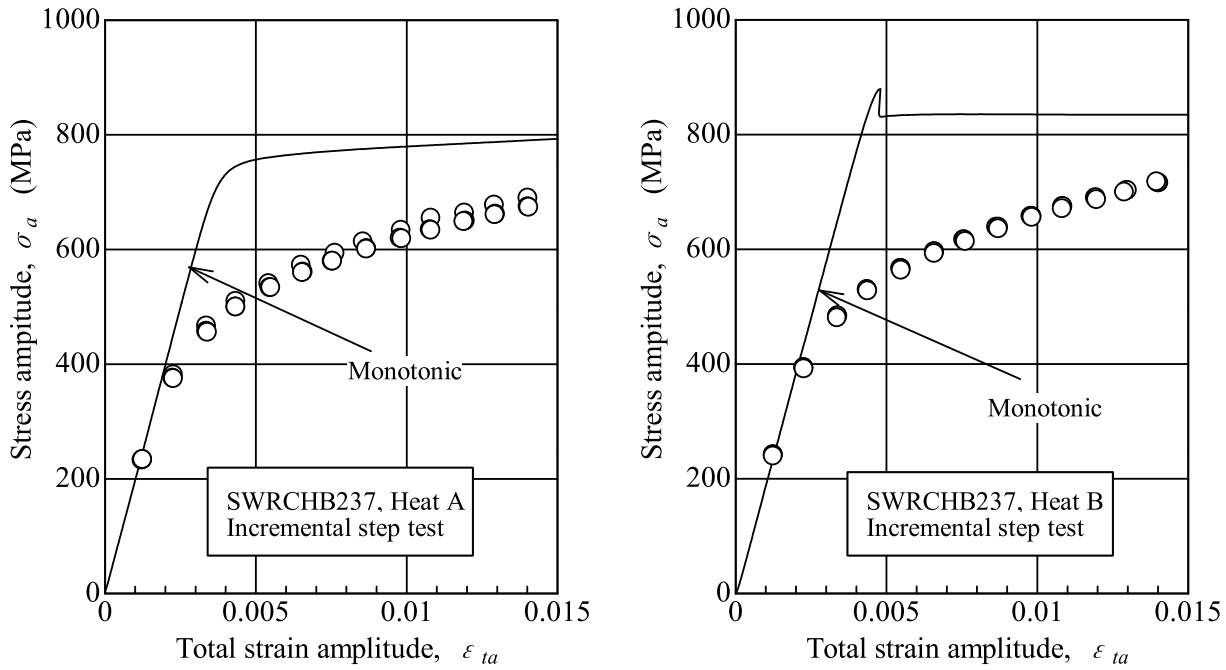

Figure 3. Cyclic stress-strain diagram obtained by incremental step tests on the boron steel samples.

Table 7. Cyclic stress-strain properties[1] of the boron steel samples. C' and n' : exponent and coefficient (MPa) in cyclic stress-strain relation $\sigma_a = C'\varepsilon_{pa}{}^{n'}$, by incremental step tests. σ_a : stress amplitude (MPa), ε_{pa} : plastic strain amplitude, σ_{yc} : cyclic yielding stress.

Heat	C'	n'	σ_{yc}
A	1487	0.171	515
B	1476	0.160	547

[1]Cyclic properties were determined by linear regression analysis of log σ_a to logε_{pa} for total strains less than 1.4×10^{-2}. Extrapolation is not recommended.

cyclic yield stress σ_{yc} and tensile strength σ_B was close to $\sigma_{yc} = 0.61\sigma_B$.

Figure 5 shows the results of constant-strain amplitude tests. The total strain amplitudes were divided into plastic and elastic strain amplitudes. The plastic and elastic strain amplitudes were at half of the fatigue lives. At high total strain amplitudes, the plastic strain amplitudes were higher than the elastic strain amplitudes; however, this relationship was reversed at low total strain amplitudes. The crossing points were at around 0.6% of total strain amplitudes and at around 10^3 or 10^4 cycles of the fatigue lives. The regions in which plastic strain amplitudes exceeded the elastic strain amplitudes were 'low-cycle fatigue regions' subject to the Manson-Coffin law. Figure 6 shows cyclic softening

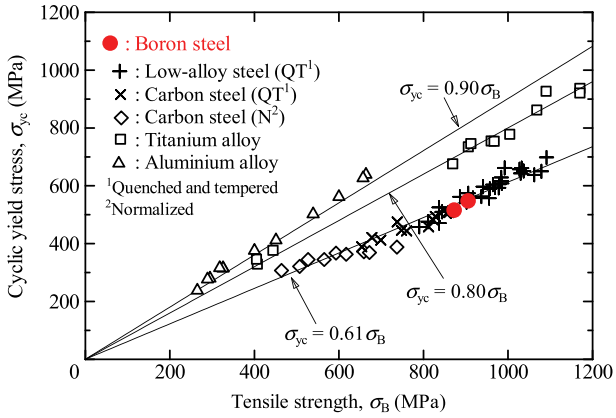

Figure 4. Comparison of cyclic yield stress between the boron steel samples and other materials.

were at half of the fatigue lives. The boron steel samples revealed cyclic softening. Table 7 shows the models for their cyclic stress-strain curves. Figure 4 shows the comparison of cyclic yield stress between the boron steel samples and other materials. The cyclic yield stress of the boron steel showed good agreement with that of other steels. The relationship between

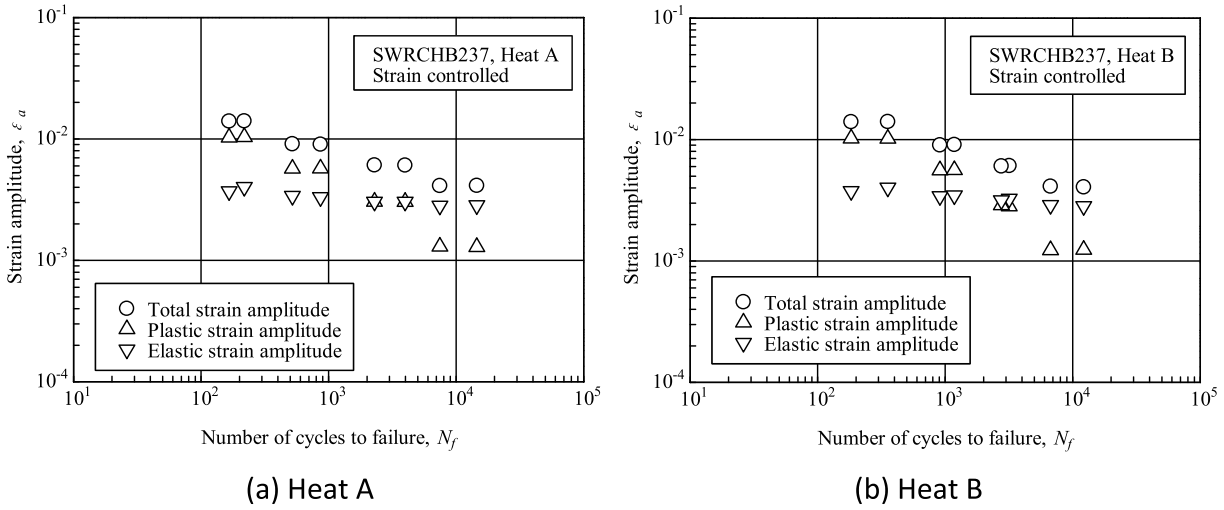

(a) Heat A (b) Heat B

Figure 5. *S-N* diagram showing the constant-strain amplitude fatigue properties of the boron steel samples.

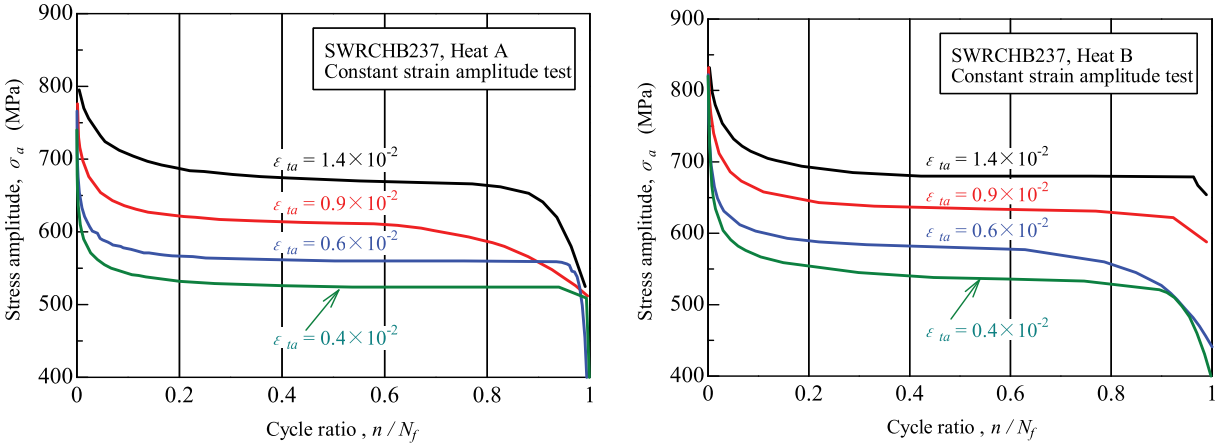

Figure 6. Changes in stress amplitude during constant-strain amplitude fatigue tests of the boron steel samples.

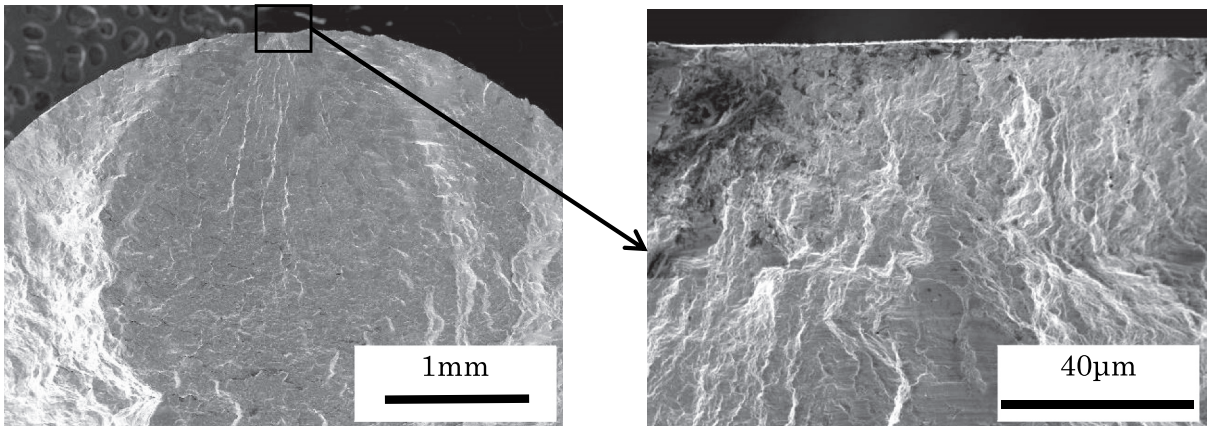

(a) Heat A, constant-strain amplitude test (ε_{ta} = 0.61x10^{-2}, N_f = 3.98×10^3 cycles)

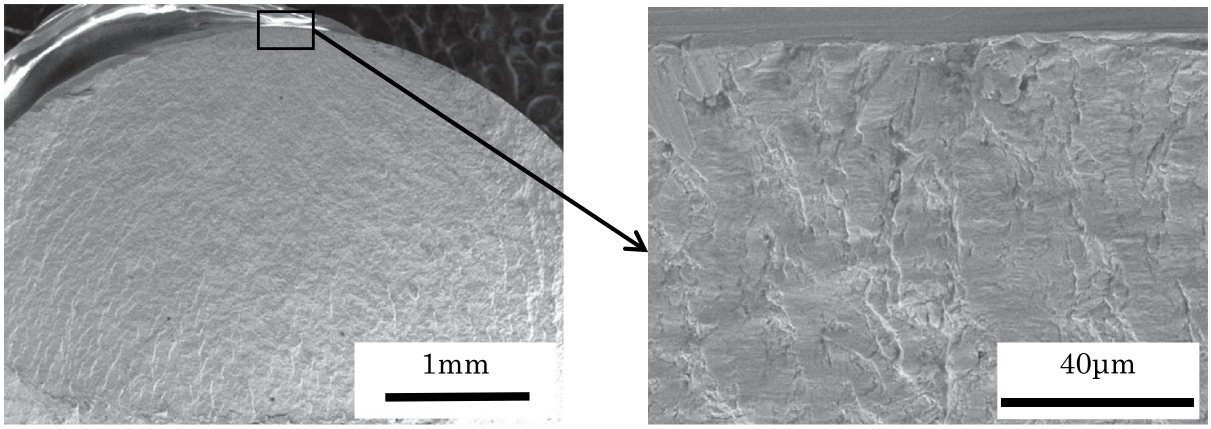

(b) Heat B, constant-strain amplitude test (ε_{ta} = 0.41x10^{-2}, N_f = 6.70×10^3 cycles)

Figure 7. Typical fracture surfaces obtained by the low-cycle fatigue tests.

curves. Cyclic softening occurred very early and saturated after 10% of fatigue life. Figure 7 shows typical fracture surfaces after constant-strain amplitude testing. The fatigue cracks initiated at surfaces, and the fracture surfaces revealed typical transgranular fatigue fracture morphologies.

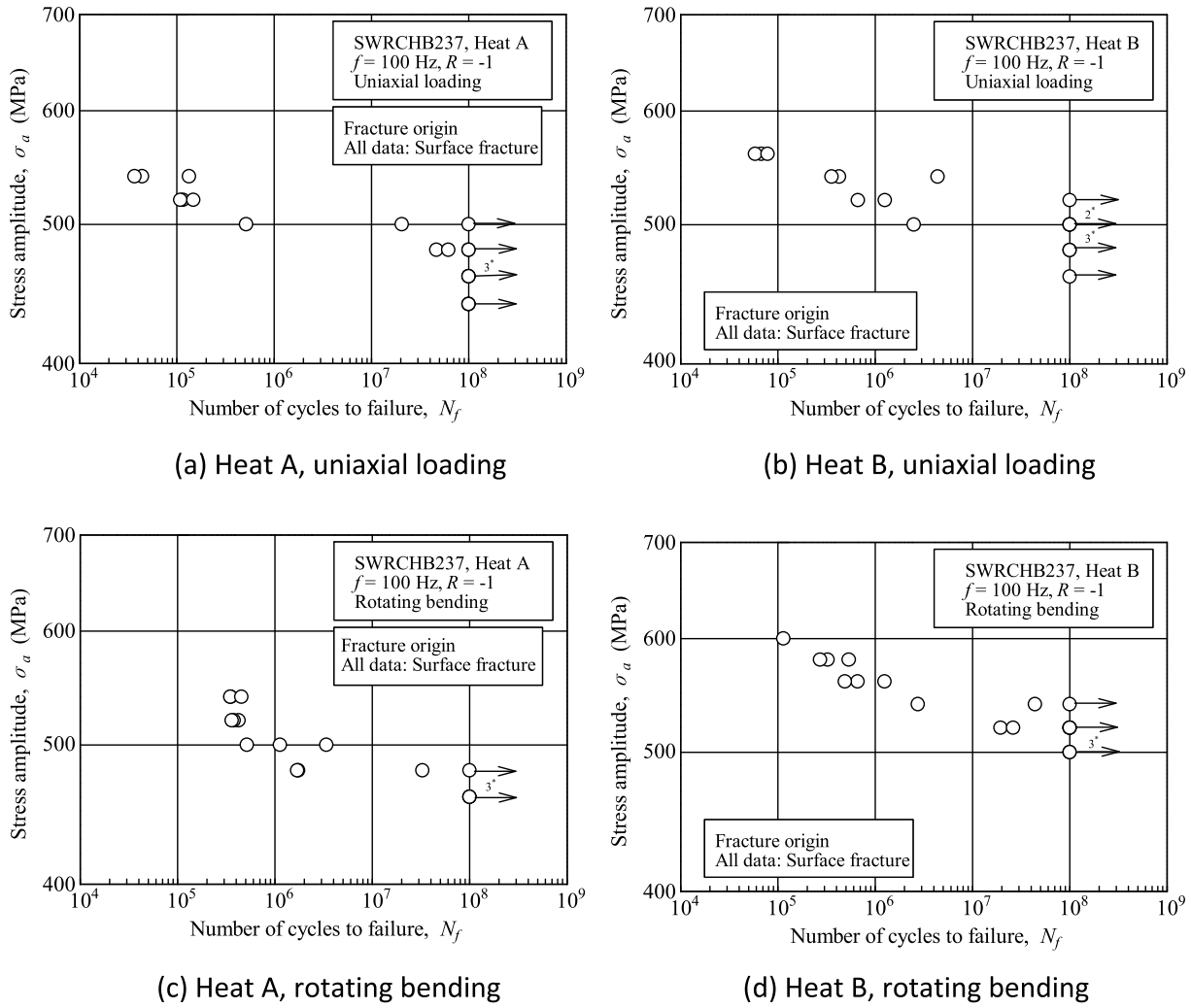

Figure 8. *S-N* diagram showing the high-cycle fatigue properties of the boron steel samples.

3.2. High-cycle fatigue test results

Figure 8 shows the results of the high-cycle fatigue tests. Heat B revealed slightly higher fatigue strength due to its higher tensile strength. Only a small difference between uniaxial loading and rotating bending results was apparent. Several specimens fractured at over 10^7 cycles, so the fatigue limits were not clear. No internal fractures were observed, however, with all specimens ending in surface fractures.

Figure 9 presents *S-N* diagrams that show both low- and high-cycle fatigue test results. The stress amplitudes of the low-cycle fatigue tests were at half of the fatigue lives. The high-cycle fatigue test results were continuously related to the low-cycle fatigue test results, whereas the low-cycle fatigue test results revealed slightly shorter fatigue lives that were attributed to cyclic softening of the boron steel. In cases where cyclic softening occurred, the initial stress amplitudes of the constant-strain amplitude tests were higher than those of the high-cycle fatigue tests.

Table 8 shows numerical values of 10^8-cycle fatigue strengths. The fatigue strengths are average values between the maximum stress amplitude at which no specimen is fractured, and that just above it.

Figure 10 shows a comparison of fatigue strengths as measured by rotating bending fatigue tests and by uniaxial loading fatigue tests. The low-strength steels reveal stress gradient effects in which rotating bending fatigue testing results in higher fatigue strengths than uniaxial loading fatigue testing. The stress gradient effects are lower in high-strength steels, and the difference between rotating bending and uniaxial loading becomes very small when tensile strengths exceed 800 MPa. The tensile strengths of the boron steel samples are distributed around 900 MPa, which is why the difference between the rotating bending results and the uniaxial loading results is small in the boron steel samples.

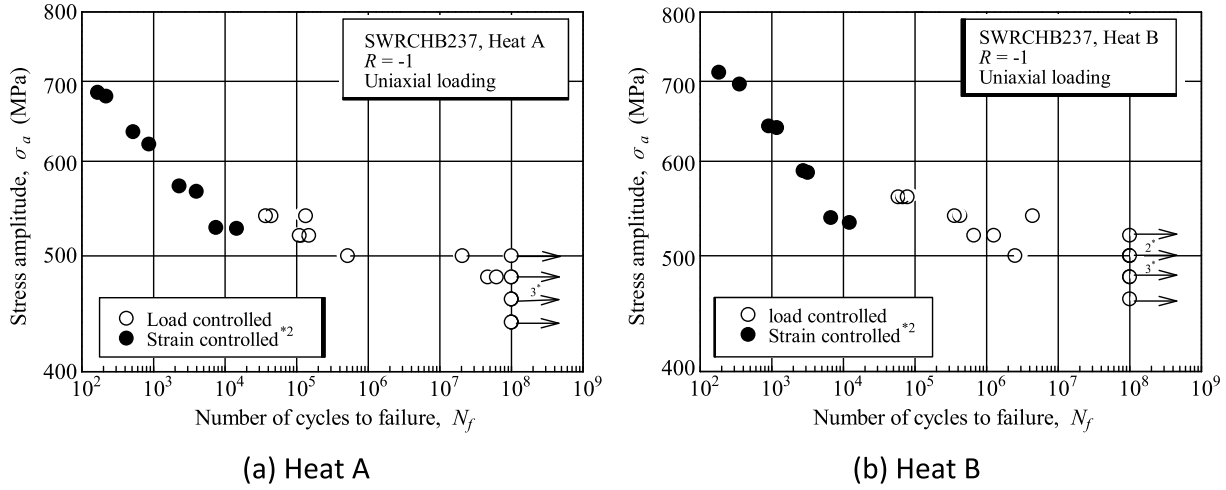

∗: Number of overlapped specimens
∗2: Stress amplitude at the N_f / 2

Figure 9. *S-N* diagram showing the constant-strain or constant-stress amplitude fatigue properties of the boron steel samples.

Table 8. Estimated mean fatigue strengths[1] of the boron steel samples at 10^8 cycles (stress amplitude in MPa).

Heat	Uniaxial loading	Rotating bending
	10^8 cycles	
A	470	470
B	490	510

[1]The fatigue strengths are average value between the maximum stress amplitude at which no specimen is fractured and the stress amplitude just above it.

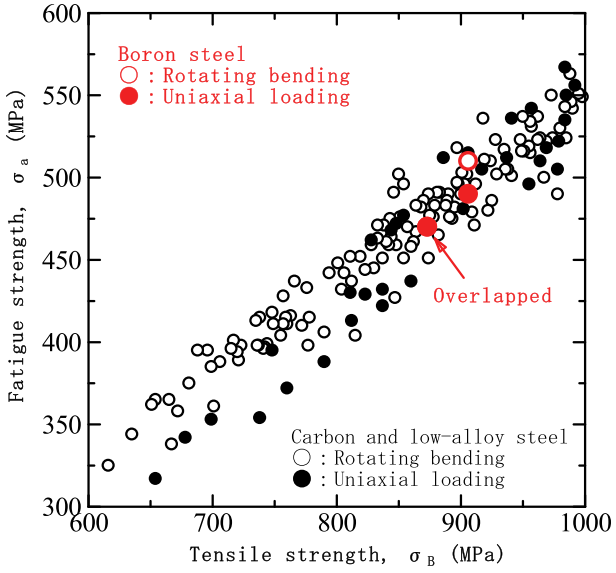

Figure 10. Comparison of fatigue strengths between rotating bending and uniaxial loading fatigue tests.

Figure 11 shows a comparison of fatigue strengths between the boron steel samples and other steels. The fatigue strengths of the boron steel show good agreement with those of the quenched and tempered low-alloy steels.

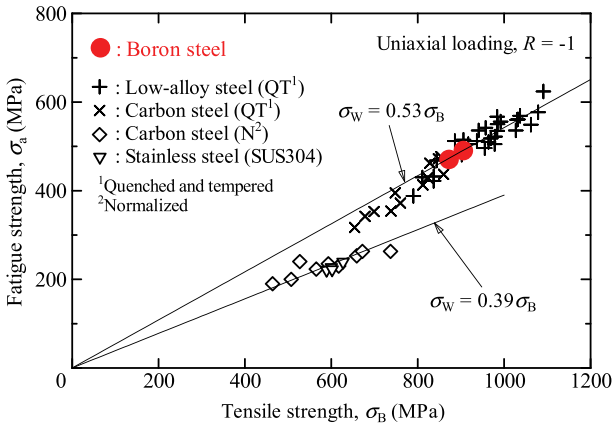

Figure 11. Comparison of fatigue strengths between the boron steel samples and other steels under uniaxial loading.

Figure 12 shows typical fracture surfaces obtained in the high-cycle fatigue tests. The fatigue cracks initiated at surfaces, and the fracture surfaces revealed typical transgranular fatigue fracture morphologies.

4. Discussion

The chemical composition of boron steel is very close to that of carbon steels such as JIS-S40C. The major difference is the addition of a trace of boron (≈0.002%). This tiny amount of boron dramatically increases the hardenability of carbon steel. Past fatigue data sheets [3–7] applied water-quenching to carbon steel, since martensite was not obtained by conventional oil-quenching. The boron steel samples, however, revealed very fine martensite after oil-quenching (Figure 1). The fatigue performance of the boron steel samples was very close to that of low-alloy steel. Cyclic yield stress (Figure 4) and fatigue strength (Figure 11) of the boron steel were comparable to those of the low-

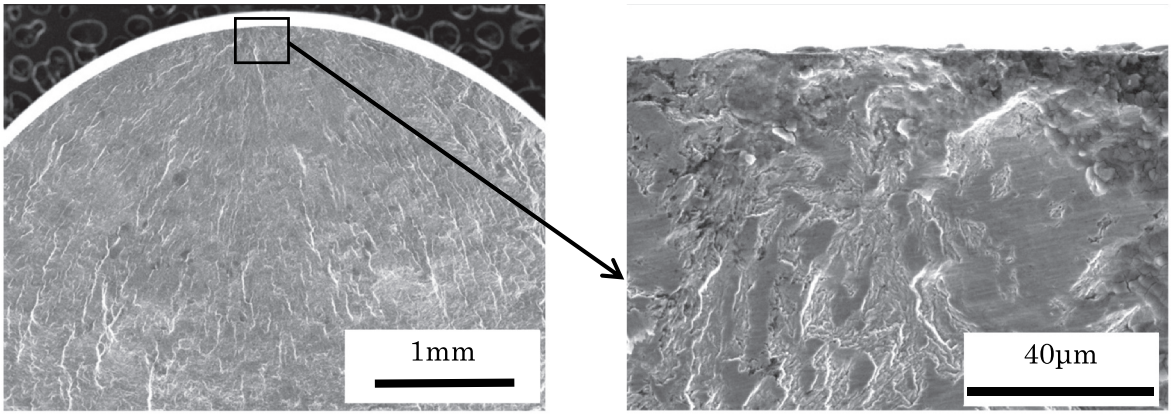

(a) Heat A, uniaxial loading (σ_a = 500 MPa, N_f = 2.06 × 10^7 cycles)

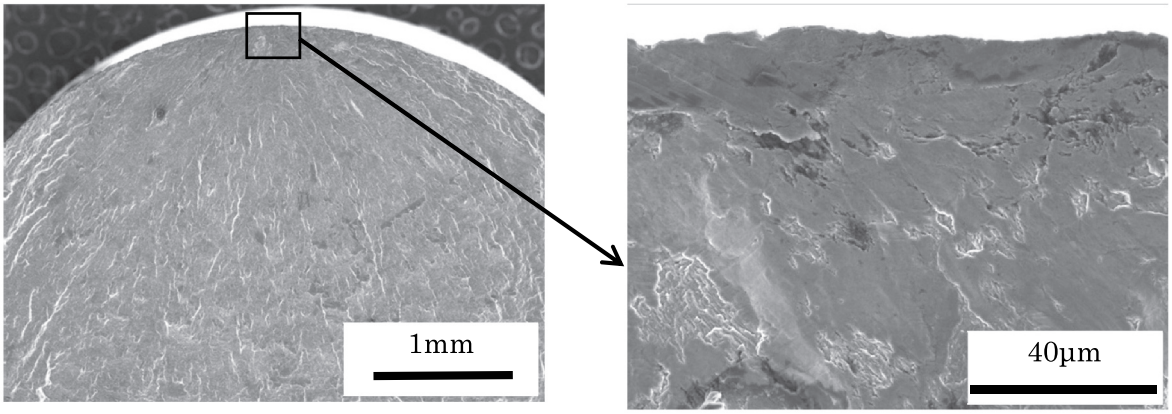

(b) Heat A, uniaxial loading (σ_a = 500 MPa, N_f = 5.17 × 10^5 cycles)

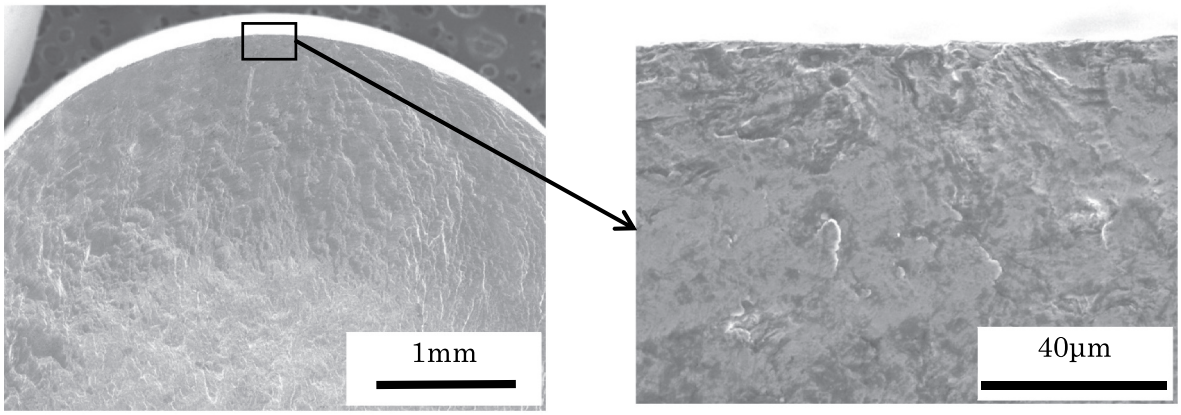

(c) Heat A, rotating bending (σ_a = 500 MPa, N_f = 1.13 × 10^6 cycles)

Figure 12. Typical fracture surfaces obtained in the high-cycle fatigue tests.

alloy steel. As shown in Figure 11, the fatigue strength of the low-alloy steel is slightly higher than that of the water-quenched carbon steel, i.e. the low-alloy steels (+) show good agreement with the $\sigma_W = 0.53\sigma_B$ line, while the water-quenched carbon steels (×) were lower than the $\sigma_W = 0.53\sigma_B$ line. The boron steel samples then matched the low-alloy steel. The boron steel samples thus show excellent hardenability, resulting in high fatigue performance. Further research is necessary to clarify the detailed mechanisms. One difference from the low-alloy steel is resistance to temper softening. The tensile strength of boron steel is thus lower than that of low-alloy steels such as JIS-SCM440.

Another point to be noted is the long-life fatigue failure at above 10^7 cycles without internal fracturing. Long-life surface fractures were also seen in carbon steels [6] and low-alloy steels [8] at above 10^8 cycles, whereas they did not occur in high-speed ultrasonic fatigue tests at 20 kHz [7,9]. Our understanding is, therefore, that long-life surface fracturing might be

attributable to corrosion effects by air [10,11]. Corrosion pits were not confirmed on the fracture surface, so such corrosion effects must be very subtle. For example, non-propagating cracks begin to grow again due to slight corrosion effects. The slight corrosion might destroy dislocation-dense areas of crack tips at surfaces, which re-start the crack growth at surfaces, followed by the crack growth into interiors. Long-life surface fracturing is a potential future subject of research.

5. Summary

The NIMS fatigue data sheet No. 134 discloses low- and high-cycle fatigue test results for boron steel samples. The low-cycle fatigue tests under strain-controlled conditions were of two types: incremental step tests to clarify cyclic stress-strain curves and constant-strain amplitude tests to clarify fatigue lives. The high-cycle fatigue tests consisted of a uniaxial loading type and a rotating bending type at 100 Hz.

The incremental step tests revealed that cyclic softening occurred in the boron steel samples. The cyclic yield stress was then identical to that of other steels. In the constant-strain amplitude tests, the plastic strain amplitudes were higher than the elastic strain amplitudes when the total strain amplitudes were above 0.6%. The crossing points appeared at around 10^3 or 10^4 cycles of the fatigue lives. This means that the Manson-Coffin law is applicable to boron steel provided that its fatigue life is below 10^3 or 10^4 cycles.

The high-cycle fatigue tests revealed the fatigue strength to be slightly different between heats due to differences in tensile strength. Differences between the test types (uniaxial loading and rotating bending) were small. The fatigue strength of the boron steel samples was more comparable to that of low-alloy steel than to that of carbon steel. Boron steel thus revealed high fatigue performance arising from its excellent hardenability. The fatigue limits were not clear, since several specimens fractured at over 10^7 cycles without showing any internal fracturing. Our understanding is that the observed long-life surface fracturing could be attributable to very mild corrosion effects caused by ambient air. This effect could potentially be the subject of a future research study.

Disclosure statement

No potential conflict of interest was reported by the author(s).

References

[1] Furuya Y, Nishikawa H, Hirukawa H, et al. Catalogue of NIMS fatigue data sheets. Sci Technol of Adv Mater (STAM). 2019;20(1):1055–1072. doi: 10.1080/14686996.2019.1680574
[2] Landgraf RW, Morrow J, Endo T. Determination of cyclic stress-strain curve. J Mater. 1969;4:176–188.
[3] Furuya Y, Nishikawa H, Hirukawa H, et al. Data sheets on fatigue properties of S35C (0.35C) steel for machine structural use, NRIM fatigue data sheet, No. 2. Tokyo: National Research Institute for Metals; 1978. doi: 10.11503/nims.1066
[4] Furuya Y, Nishikawa H, Hirukawa H, et al. Data sheets on fatigue properties of S45C (0.45C) steel for machine structural use, NRIM fatigue data sheet, No. 3. Tokyo: National Research Institute for Metals; 1978. doi: 10.11503/nims.1067
[5] Furuya Y, Nishikawa H, Hirukawa H, et al. Data sheets on fatigue properties of S55C (0.55C) steel for machine structural use, NRIM fatigue data sheet, No. 4. Tokyo: National Research Institute for Metals; 1978. doi: 10.11503/nims.1068
[6] Furuya Y, Nishikawa H, Hirukawa H, et al. Data sheets on giga-cycle fatigue properties of S40C (0.40C) carbon steel for machine structural use, NIMS fatigue data sheet, No. 97. Tsukuba: National Institute for Materials Science; 2005. doi: 10.11503/nims.1161
[7] Furuya Y, Nishikawa H, Hirukawa H, et al. Data sheets on ultrasonic fatigue properties of S40C (0.40C) carbon steel for machine structural use, NIMS fatigue data sheet, No. 102. Tsukuba: National Institute for Materials Science; 2007. doi: 10.11503/nims.1166
[8] Furuya Y, Nishikawa H, Hirukawa H, et al. Data sheets on giga-cycle fatigue properties of SCM440 (0.40C-1Cr-0.2Mo) steel for machine structural use, NIMS fatigue data sheet, No. 104. Tsukuba: National Institute for Materials Science; 2008. doi: 10.11503/nims.1168
[9] Furuya Y, Nishikawa H, Hirukawa H, et al. Data sheets on ultrasonic fatigue properties of SCM440 (0.40C-1Cr-0.2Mo) steel for machine structural use, NIMS fatigue data sheet, No. 106. Tsukuba: National Institute for Materials Science; 2009. doi: 10.11503/nims.1170
[10] Abe T, Furuya Y, Hirukawa H. Giga-cycle fatigue properties of induction hardened 0.40% C carbon steels. Tetsu-To-Hagane. 2007;93(12):775–781. doi: 10.2355/tetsutohagane.93.775
[11] Furuya Y, Abe T, Takeuchi E, et al. Ultrasonic fatigue properties of high-strength materials, NIMS fatigue data sheet technical document No. 19. Tsukuba: National Institute for Materials Science; 2013.